Contents lists available at ScienceDirect

Applied Surface Science

journal homepage: www.elsevier.com

Full Length Article

Magnetism and multiferroic properties at $MnTiO_3$ surfaces: A DFT study

Renan A.P. Ribeiro[a], Juan Andrés[b,*], Elson Longo[c], Sergio R. Lazaro[a]

[a] Department of Chemistry, State University of Ponta Grossa, Av. General Carlos Cavalcanti, 4748, 84030-900 Ponta Grossa, PR, Brazil
[b] Department of Analytical and Physical Chemistry, University Jaume I (UJI), Castelló 12071, Spain
[c] CDMF-UFSCar, Universidade Federal de São Carlos, PO Box 676, 13565–905 São Carlos, SP, Brazil

ARTICLE INFO

Keywords:
$MnTiO_3$
Magnetism
Multiferroic properties
Morphology
Wulff's construction
Surface energy
Spin density

ABSTRACT

The present study illustrates how density functional theory calculations can rationalize the surface structure and magnetism for the low-index (1 1 0), (1 0 1), (1 0 0), (0 0 1), (1 1 1), and (0 1 2) surfaces of $MnTiO_3$. A simple procedure, without surface reconstructions or chemical adsorptions in which the stability, magnetism and the morphological transformations is presented in detail to clarify the control of their multiferroic nature. The surface stability was found to be controlled by the octahedral $[MnO_6]$ and $[TiO_6]$ clusters formed by the Mn^{2+} and Ti^{4+} cations - i.e., their local coordination at the surfaces, respectively- with nonpolar (1 1 0) being the most stable. Enhanced superficial magnetism was found for (0 1 2), (0 0 1), and (1 1 1) surfaces in agreement with the more undercoordinated $[TiO_n]'$ and $[MnO_n]^{\bullet}$ complex clusters at the surface plane. Our calculation suggests the existence of magnetic $[TiO_n]'$ species for unstable (0 0 1) and (1 1 1) surfaces, explained by the unusual crystal-field associated with the surface environment. The crystal morphology has been predicted to determine the most likely terminations to be present as well as the intrinsic magnetization density associated with morphologies. Moreover, the (0 0 1) surface plane plays a key role in the enhancement of the magnetic properties for shape-oriented $MnTiO_3$ nanoparticles, suggesting a superior magnetoelectric coupling due to the presence of uncompensated spins and polar distortions perpendicular to the surface plane.

1. Introduction

Polar oxides, such as ferroelectric materials, have been widely investigated in recent years owing to the potential technological applications in the development of advanced devices [1]. In addition, several studies have exploited the electrical field at the ferroelectric surfaces, indicating that the surface polarity can be switched by an external electric field that controls the bulk spontaneous polarization [1–3]. In this case, the chemical and physical properties associated with the surfaces can be controlled, resulting in several interesting applications—for instance, the dynamic control of catalysis, photocatalysis and artificial photosynthesis, and switchable chemical sensors [3–11].

The manipulation of multiferroic surfaces—widespread candidates for spintronic-based technologies—becomes more intriguing owing to the coupling between magnetic and ferroelectric orders [12]. In this context, a plethora of theoretical and experimental efforts have been devoted to investigating a wide range of multiferroic materials, with $BiFeO_3$ being the most reported candidate owing to the large ferroelectric polarization associated with G-type antiferromagnetic order [13]. The first study on the properties of $BiFeO_3$ surfaces was developed by Zhu et al., in which the stability and electronic structure of a polar (1 1 1) surface was resolved from density functional theory (DFT) calculations, showing marked differences with respect to the bulk [14]. More recently, Shimada et al. reported the chemical nature of nonpolar (1 1 0) surfaces of $BiFeO_3$ through DFT + U calculations, suggesting that the unique surface magnetoelectric response is associated with the distinct rotation pattern of ferroelectric polarization from the breaking symmetry addressed to the surfaces [15]. Further, Dai et al. performed systematic DFT + U calculations to study the nature, thermodynamic stability, and ferroelectric-induced Pd adsorption on the $BiFeO_3$ (0 0 0 1) polar surfaces. The main observations of these authors are focused on the different chemical natures of positive and negative surface terminations, which exhibit an enhanced relation between spontaneous polarization and weak ferromagnetism as well as distinct behavior as a substrate for metal adsorption, suggesting the intriguing catalytic properties of the metal/$BiFeO_3$ interface [16–18].

* Corresponding author.
Email address: andres@qfa.uji.es (J. Andrés)

https://doi.org/10.1016/j.apsusc.2018.05.067
Received 19 April 2018; Accepted 9 May 2018
Available online xxx
0169-4332/

Transition metal titanates $ATiO_3$ (A = Mn, Fe, Ni), with a $LiNbO_3$-type (R3c) structure, are among the most promising multiferroic materials owing to their remarkable magnetoelectric coupling. These compounds are structurally isomorphic to $BiFeO_3$ except that the positions of A and B cations are exchanged [19,20]. In the past few years, the scientific interest in such materials has increased owing to the possibility of controlling the magnetism from antisymmetric Dzyaloshinskii-Moriya interaction [20–24]. In a previous work, we successfully described the multiferroic properties of such materials using DFT calculations [25]. The *R3c* structure consists of oxygen layers in a distorted hexagonal close-packed configuration, in which the octahedral local coordinations—i.e., $[AO_6]$ and $[TiO_6]$ clusters—are equally occupied by A and Ti cations, following the order Ti-vac-A-Ti-vac-A, as depicted in Fig. 1. Below the Curie temperature, the A cations are displaced from the central positions of oxygen octahedral cages—i.e., $[AO_6]$ cluster—resulting in a spontaneous polarization along the (0 0 1) direction [10,19]. This distortion also induces a singular crystal-field splitting, especially for A-site cations, owing to the existence of a trigonal prismatic arrangement (D_{3h}) that splits the t_{2g} levels into nondegenerated a_{1g} and double-degenerated e_g^{π} states, whereas e_g becomes e_g^{σ}. In contrast, the smallest distortion degree associated with $[TiO_6]$ clusters maintain the octahedral crystal-field distribution (O_h). Despite the current theoretical studies developed for $ATiO_3$ (A = Mn, Fe, Ni) materials, the intrinsic physical and chemical properties of the surfaces remain unclear [20–24,26,27].

Recently, $MnTiO_3$, as a representative antiferromagnetic semiconductor of the ilmenite family, is the main subject in the multiferroics area owing to the potential magnetoelectric effect [24,26]. $MnTiO_3$ exhibits a weak ferromagnetism below the Néel temperature, $T_N = 28$ K, which is perpendicular to the electrical polarization resulting from cation displacement enabling the switches of two ferroic properties. Furthermore, magnetodielectric measurements indicate a dielectric anomaly at T_N when a magnetic field is applied along the c axis, giving rise to a linear magnetoelectric coupling [24,26]. A note of caution is mandatory here, multiferroic materials such as $MnTiO_3$ would exhibit non-collinear spin ordering at the surface, probably associated with the formation of magnetic domains. The description of such effects s beyond the scope of the present paper.

In this study, we seek to fulfill a twofold objective. First, we provide detailed information on the surface energies of the (1 0 0), (1 1 0), (1 0 1), (0 0 1), (1 1 1), and (0 1 2) surfaces of $MnTiO_3$ material obtained from DFT calculations. Second, a microscopic interpretation of the changes in the values of the surface energies are related with the number of unpaired electrons per surface in order to determine the magnetization of different morphologies. We believe that these novel results can arouse enough interest because they contribute to broadening the fundamental knowledge on the multiferroic nature of the $MnTiO_3$ associated with polar and nonpolar surfaces.

The rest of the paper is divided into three sections. In the next section, we describe in detail the computational methodology. Section 3 contains the results and discussion divided into three main subsections. The first subsection addresses the surface energies and relaxations. The second presents our analysis of the surface electronic and spin properties, whereas the superficial magnetism and crystal morphology are presented in the third subsection. The paper ends with the main conclusions of our work.

2. Computational methodology

To investigate the multiferroic properties associated with the surfaces of $MnTiO_3$, a slab construction model was employed. In this case, the chemical structure of the surface was described by a two-dimensional periodic film formed by atomic layers parallel to the (*hkl*) crystalline plane of interest, cut from the optimized bulk geometry [25]. Here, (1 0 0), (1 1 0), (1 0 1), (0 0 1), (1 1 1), and (0 1 2) surface planes were considered, enabling the structure of polar and nonpolar surfaces and its effects on the multiferroic properties to be explored.

The purpose of this paper is to introduce in the simplest possible terms the apparent difficulties associated with defining polarization in bulk solids [28]. Upon examining the atomic layers of the planes, it was observed that (1 1 0) is non-polar ($\mu_z = 0$), whereas (1 0 0), (0 0 1), (1 0 1), (1 1 1) and (0 1 2) generates polar surfaces due to the ferroelectric polarization containing two slab terminations, which cannot be made equivalent. The purpose of this paper is to introduce in the simplest possible terms the apparent difficulties associated with defining polarization in bulk solids. Then, we use a theoretical procedure to explore the surface energies without surface reconstructions or chemical adsorptions commonly used to cancel the macroscopic dipole and stabilize the Type-3 Tasker's surface, as proposed by Dai and co-authors [16–18]. First, we introduce the unrelaxed cleavage energy (E_{cleav}^{unrlx}) of the complementary terminations (Z^+ and Z^-), as the required energy to cut the crystal into two unrelaxed complementary terminations, as follows:

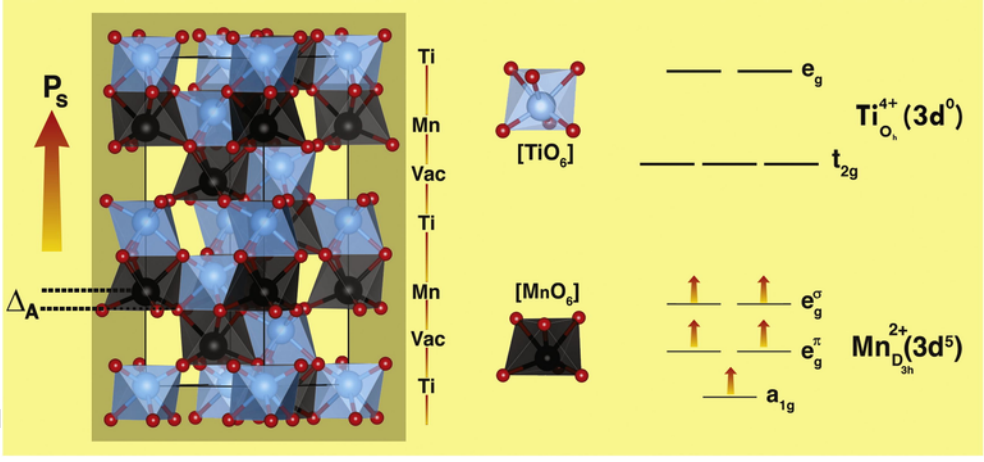

Fig. 1. Conventional crystallographic unit cell (R3c) for $MnTiO_3$. The black, blue, and red balls represent Mn, Ti, and O ions, respectively. The blue and black polyhedral represent the octahedral $[TiO_6]$ and $[MnO_6]$ clusters, respectively. Δ_A correspond to the atomic displacement with respect to the paraelectric structure, which originates the spontaneous polarization (P_s) along the z-axis. The right panel describes the local structures for $[TiO_6]$ and $[MnO_6]$ clusters and corresponding crystal-field diagrams. (For interpretation of the references to colour in this figure legend, the reader is referred to the web version of this article.)

$$E_{cleav}^{unrlx} = \frac{\left(E_{slab}^{unrlx} - nE_{bulk}\right)}{2A} \quad (1)$$

Here, E_{slab}^{unrlx} and E_{bulk} correspond to the total energies for the unrelaxed slab model and the bulk unit, whereas n and A represent the number of bulk units used in the slab construction and the surface area, respectively.

In the next step, the relaxation of the complementary terminations (Z^+ and Z^-) was performed, considering that only the outer $MnTiO_3$ layers were allowed to relax while the inner positions were clamped to reproduce the bulk [16–18]. The unrelaxed cleavage energy (E_{cleav}^{relax}) was then computed as:

$$E_{relax} = \frac{\left(E_{slab}^{unrlx} - E_{slab}^{relax}\right)}{A} \quad (2)$$

$$E_{cleav}^{relax} = E_{cleav}^{unrlx} - E_{relax} \quad (3)$$

These approaches have been successfully applied to investigate the surface properties for many kinds of materials [29–35]. Here, it is important to note that cleavage energy is helpful to understand the energy cost to cut a singular surface focusing on the cleaved bonds and superficial metal coordination; the relaxed surface energies account for the local relaxations that contribute to increasing the surface stability. The convergence test for the values of the surface energies with slab thickness was performed for all surfaces. After the corresponding optimization process and thickness convergence tests, the repeat units {number of layers in the slab} are selected as Ti—O_3—Mn— {18 layers} for (0 0 1), O_3—Mn_2Ti_2—O_3 {40 layers} for (1 1 0), O—Ti—O—Mn—O {30 layers} for (1 0 1), and O_2—Mn_2—O_2—Ti_2—O_2 {30 layers} for (0 1 2), O_2—Mn_2Ti_2—O_4 {40 layers} for (1 0 0) and O—Ti—O—Mn—O—Ti—O_2—Mn—O {50 layers} for (1 1 1) with surface terminations giving rise to a minimal dipole moment, although different surface terminations may occur. These numbers of layers were found to be sufficient for a convergence of the results. In the course of the geometry optimization, we do not place any constraints on the atoms except for the conservation of the original crystal symmetry in the two dimensions parallel to the surface.

$MnTiO_3$ crystallizes in the acentric $LiNbO_3$-type structure, showing a G-type antiferromagnetic order. In our previous work [25], the bulk structure was represented by two collinear magnetic configurations using the primitive (10-atoms) unit cell: (i) ferromagnetic (FEM), where the spins for all neighbors are parallel ordered; (ii) antiferromagnetic (AFM) for which the spins on the nearest neighbors are antiparallel ordered to each other. Here, we consider the FEM structure containing two spin-up symmetry related Mn atoms in the primitive cell in order to reduce the computational cost for the slab optimization process. In addition, single-point calculations based on the optimized FEM structure for the slab were performed to describe the experimental AFM ordering.

All calculations were performed using the CRYSTAL14 [36] code with PBE0 [37] hybrid functional. Mn, Ti, and O centers were described from all-electron atomic basis sets composed of Gaussian type functions denominated 86-411d41G, 86-51(3d)G, and 8-411, respectively [38–40]. It is important to recognize that the electron correlation effects are important in manganite materials, but we are confident in our results because the computed bulk structural properties and bandgaps of $MnTiO_3$ are in agreement with experimental results [25]. Diagonalization of the Fock matrix was performed at adequate k-point grids (Pack–Monkhorst) in the reciprocal space [41]. The thresholds controlling the accuracy of the Coulomb and exchange integral calculations were controlled by five thresholds set to 7, 7, 7, 7, and 14. The irreducible Brillouin zone (IBZ) was represented by a number of sampling points, which are chosen as (8×8×8) and (4×4) for the bulk and slab, respectively. As a result, there are 65k -points in the bulk IBZ and 4k -points in the slab IBZ. The convergence criteria for mono- and bielectronic integrals were set to 10^{-8} Hartree, and the RMS gradient, RMS displacement, maximum gradient, and maximum displacement were set to 3×10^{-5}, 1.2×10^{-4}, 4.5×10^{-5}, and 1.8×10^{-4} a.u., respectively.

3. Results and discussions

3.1. Surface energies and relaxations

The values of the unrelaxed calculated cleavage, E_{cleav}^{unrlx}, their decreasing after optimization process, E_{relax}, and the relaxed calculated cleavage, E_{cleav}^{relax} for each surface are given in Table 1.

Considering the values for E_{cleav}^{unrlx}, the observed stability order is (1 1 0) > (0 1 2) > (1 0 1) > (1 0 0) > (0 0 1) > (1 1 1). An analysis of the results reported in Table 1 shows that the smallest values of E_{cleav} are associated with the presence of 5-coordinated Mn and Ti local environments corresponding to the undercoordinated [MnO_5] and [TiO_5] clusters, respectively, for nonpolar (1 1 0) and polar (0 1 2) surfaces, whereas a higher local undercoordination for both Mn and Ti centers results in large values of E_{cleav}.

For calculating the values of the relaxed cleavage energies, E_{cleav}^{relax}, we must consider the complementary surfaces resulting from the cutting. In polar materials, each surface termination exhibits a singular chemical environment that enables different degrees of surface relaxation and then different electronic density redistributions. This behavior will be analyzed further in the next section. The calculated values

Table 1
Calculated energies of E_{cleav}^{unrlx}, E_{relax} and E_{cleav}^{relax}, Mn and Ti local coordination for (0 0 1), (1 0 0), (1 0 1), (1 1 0), (1 1 1) and (0 1 2) surfaces. Z^+ and Z^- correspond to the positive and negative terminations of the polar surfaces, respectively. Energy values in J/m^2.

Surfaces		E_{cleav}^{unrlx}	E_{relax} (% Relaxation)	E_{cleav}^{relax}	Coordination	
					Mn	Ti
(1 1 0)	–	2.43	1.73 (71.2%)	0.70	5	5
(0 1 2)	Z^+	2.69	0.71 (26.4%)	1.98	5	–
	Z^-		0.70 (26.0%)	1.99	–	5
(1 0 1)	Z^+	3.19	0.75 (23.5%)	2.44	4	4
	Z^-		1.58 (49.5%)	1.61	4	5
(1 0 0)	Z^+	3.21	1.08 (33.6%)	2.13	4	4
	Z^-		1.19 (37.1%)	2.02	4	4
(0 0 1)	Z^+	3.46	0.95 (27.5%)	2.51	–	3
	Z^-		0.68 (19.7%)	2.78	3	–
(1 1 1)	Z^+	4.47	0.89 (19.9%)	3.57	5, 2	5, 3
	Z^-		1.12 (25.1%)	3.35	5, 3	

of E_{cleav}^{relax} show a similar stability order obtained with E_{cleav}^{unrlx}. Here, it is important to recognize that the argument related to the number of Mn-O and Ti-O is the key factor that determines the values of both E_{cleav}^{unrlx} and E_{cleav}^{relax}, however, there is not a linear relationship between these values and the number of M—O breaking bonds for the investigated surfaces [42–44], indicating that the nature of cleaved bonds is also important to deeply understand the relative stability of both E_{cleav}^{unrlx} and E_{cleav}^{relax} [45,46].

To clarify the surface structure upon relaxation, the relation among atomic displacements, undercoordinated cations, bond distances (*Supporting Information*), and surface energies (Table 1) was investigated. The relaxed surface structures are shown in Fig. 2(a–f). Here, the comparison was based on bulk values reported in our previous work [25].

First, we considered the nonpolar (1 1 0) surface. In this case, the complementary surface terminations were equal, eliminating the resulting dipole moment perpendicular to the slab, according Type-2 Tasker's classification. The surface arrangement was described by a local coordination of fivefold Mn/Ti cations—i.e., undercoordinated [MnO_5] and [TiO_5] clusters, respectively. Upon the relaxation, the topmost and outermost oxygen anions relaxed toward the Mn and Ti cations to stabilize the fivefold atomic configuration through a slight shortening of Ti-O and Mn—O bond distances.

The (0 1 2) surface was also terminated by fivefold Mn and Ti cations—i.e., undercoordinated [MnO_5] and [TiO_5] clusters—but in opposite terminations due to the polarity on the surface. In both terminations, the O anions moved toward the metal cations to stabilize the dangling bond effect. Despite the distinct chemical character associated with Mn—O and Ti—O bonds, the cleaved bonds resulted in a similar relaxation mechanism, as highlighted in Table 1 for the E_{cleav}^{relax} values of the complementary terminations.

For (1 0 1) and (1 0 0) surfaces, a higher undercoordination degree was observed for both Mn and Ti cations. In the first case, the positive termination of the (1 0 1) slab exhibited fourfold Mn/Ti cations—i.e., [MnO_4] and [TiO_4] clusters, respectively—whereas the opposite termination had fourfold Mn and fivefold Ti cations—i.e., [MnO_4] and [TiO_5] clusters, respectively—which reflected on the reduced E_{cleav}^{relax} values of the negative termination. For the (1 0 0) surface, the positive termination had threefold Mn and fourfold Ti cations—i.e., [MnO_3] and [TiO_4] clusters, respectively—whereas the opposite termination exhibited fourfold Mn/Ti cations—i.e., [MnO_4] and [TiO_4] clusters, respectively. The largest undercoordination of the (1 0 0) surface with respect to the (1 0 1) surface resulted in a slight instability for this orientation. Furthermore, this atomic arrangement entailed larger displacements of both O and Ti ions upon the relaxation.

The (0 0 1) surface was terminated by threefold metal cations—i.e., [MnO_3] and [TiO_3] clusters—with the positive (negative) termination composed of Ti (Mn) cations. The larger undercoordination effect with respect to the bulk reflected on the calculated values of E_{cleav} before

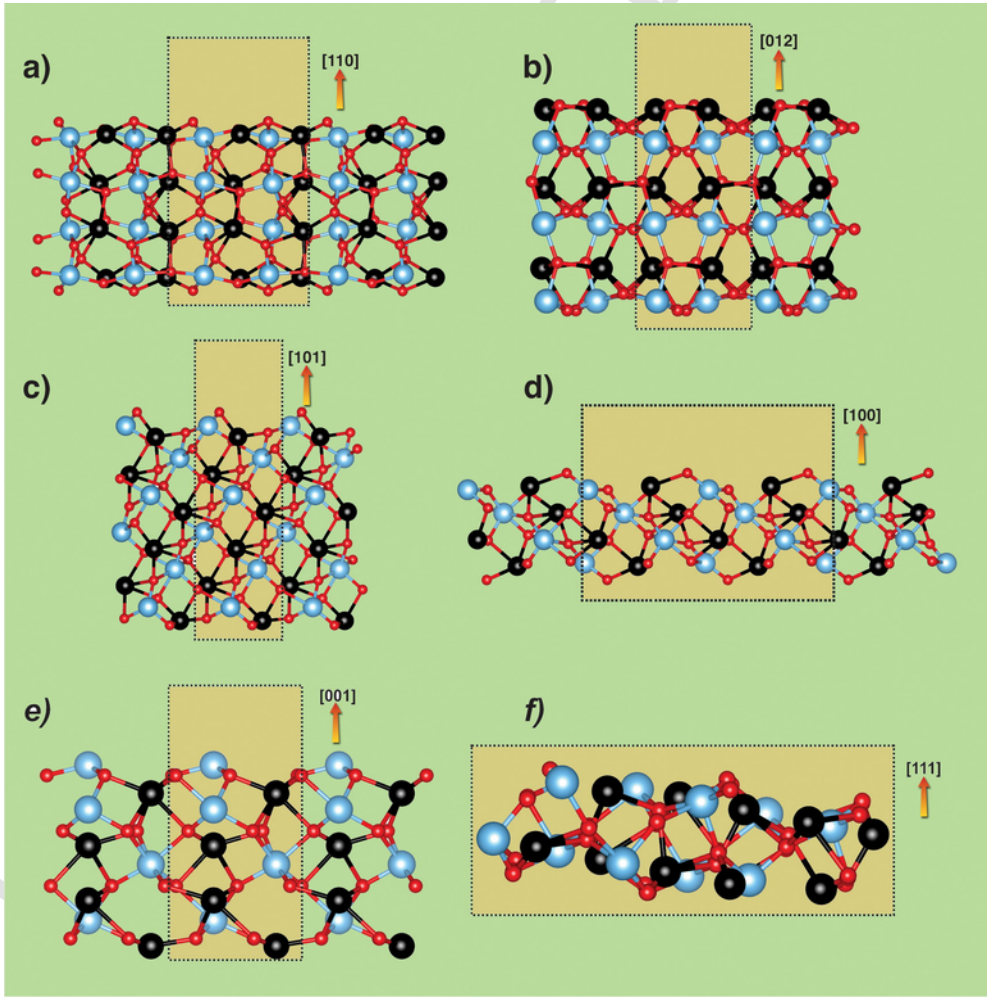

Fig. 2. Relaxed surface slabs of $MnTiO_3$. The black, blue, and red balls represent Mn, Ti, and O ions, respectively. The dashed lines represent the lattice vector used in the calculations. (For interpretation of the references to colour in this figure legend, the reader is referred to the web version of this article.)

and after the relaxation, once a larger cationic displacement was required to reduce the dangling bond effect.

The (1 1 1) surface, which had the highest values of E_{cleav}^{unrlx} and E_{cleav}^{relax} (see Table 1), exhibited Mn_{5c}, Ti_{5c}, Ti_{3c}, and Mn_{2c} cations for the positive termination, whereas along the opposite direction, we can sense the presence of Mn_{5c}, Ti_{5c}, Ti_{3c}, and Mn_{3c} cations. These arrangements require the largest cationic and anionic displacements to reduce the dangling bond effect.

3.2. Electronic and spin properties of surfaces

In this section, we discuss the electronic properties of the investigated surfaces from spin populations, charge density maps, and density-of-states projections.

Table 2 summarizes the numbers of local coordination for the Mn and Ti cations at each surface and value of the magnetic moments. In general, it was observed that the magnetic moment followed the dangling bond effect, once the surfaces with lowest coordination number for the exposed cations showed an unusual spin population compared to the bulk value (4.8) [25], as reported for other materials For instance, the nonpolar (1 1 0) and polar (0 1 2), (1 0 1), and (1 0 0) surfaces displayed the smallest deviation for the Mn magnetic moment compared to the bulk, showing that five- and fourfold configurations can stabilize the magnetic properties through a charge density rearrangement associated with the anionic displacement and shrinkage of Mn—O bond distances against the bulk (*Supporting Information*).

In contrast, for the polar (0 0 1) and (1 1 1) surfaces, an unusual spin population was observed for both positive and negative terminations, which can be directly associated with the lowest coordination number of the exposed metal cations. In the (0 0 1), the positive termination exhibited a magnetic Ti_{3c}, indicating the existence of magnetic Ti species. On the other hand, the negative termination showed a reduced magnetic moment on the Mn_{3c} center, showing the presence of high undercoordinated centers that are capable of modifying the charge density distribution along the plane. Similar behavior was observed for the (1 1 1) surface, where the existence of fivefold and threefold Mn/Ti sites resulted in a reduced spin population for Mn cations, whereas the exposed undercoordinated Ti centers became magnetic. From the viewpoint of technological applications, this mechanism is very interesting because of the possibility to induce superficial magnetism localized on nonmagnetic cations.

Table 2
Number of local coordination for the Mn and Ti cations at each surface and value of the magnetic moments.

Surface	Termination	Site	N_{coord}	Moment (μ_B)
(1 1 0)	–	Mn	5	−4.8
		Mn	5	4.8
(0 1 2)	Z^+	Mn	5	4.7
		Mn	5	−4.5
(1 0 1)	Z^+	Mn	4	4.7
	Z^-	Mn	4	−4.6
(1 0 0)	Z^+	Mn	4	−4.8
		Mn	4	4.8
	Z^-	Mn	4	−4.7
		Mn	4	4.7
(0 0 1)	Z^+	Ti	3	−0.5
	Z^-	Mn	3	−4.4
(1 1 1)	Z^+	Mn	5	−4.8
		Mn	2	4.5
		Ti	3	−0.2
	Z^-	Mn	5	4.7
		Mn	3	−3.9
		Ti	5	0.5
		Ti	3	−1.0

The existence of magnetic Ti species has been systematically investigated by means of theoretical or experimental efforts, mainly for TiO_2 [47–51]. However, several authors report the possible intervalence charge transfer $A^{2+} + Ti^{4+} \rightarrow A^{3+} + Ti^{3+}$ in ilmenite derivate materials. This mechanism was associated with the intermetallic A-O-Ti-O-A framework, which enhances the charge transfer process through the lattice deformation [52–56]. Here, the cutting process associated with the slab model for (0 0 1) and (1 1 1) surfaces induced an exposure of undercoordinated cations, promoting the charge transfer between Mn^{2+} and Ti^{4+} centers (Table 2).

To clarify the electronic features associated with magnetic Ti species along (0 0 1) and (1 1 1) surfaces, the density-of-states (DOS) projections and spin isosurfaces were analyzed, and are depicted in Fig. 3. Both surfaces exhibited an unusual electronic density distribution close to the valence band maximum (VBM). In both cases, the largest contribution of 3d orbitals for exposed Mn/Ti species mixed with 2p (O) atomic orbitals was observed in the valence band (VB). Compared with the reported DOS profile for bulk $MnTiO_3$ [25], the major differences are associated with the presence of occupied 3d Ti orbitals, confirming the existence of reduced Ti species. This mechanism is attributed to the crystal field effects associated with the undercoordinated cations, because the missing oxygen atoms along the surface plane induced a perturbation on the 3d orbital degeneracy, resulting in a pseudo-atomic orbital configuration, which enabled the location of unpaired electrons on these orbitals. In a similar way, the reduced coordination for Mn modified the t_{2g} and e_g energies, mainly for the orbitals pointing toward or closer to the *z*-axis. Furthermore, we can argue that the existence of reduced Ti species suggested an enhancement of superficial magnetism for (0 0 1) and (1 1 1) surfaces added to the reduced bandgap, compared to the bulk, indicating a surface metallization mechanism. The reordering of surface electronic density at (0 0 1) and (1 1 1) surfaces due to Mn and Ti undercoordination suggested a highly reactivity character against the other surfaces. In addition, similar results have been reported for other solid state materials, indicating that the dangling bond effect is the key to induce superficial magnetism from spin transition at magnetic and nonmagnetic cations [57,58].

Moreover, the observed DOS results were confirmed by the spin isosurfaces (Fig. 3b, d), indicating that threefold Ti cations exhibited a spin population that was fundamental to increase the magnetic moment perpendicular to the surface plane. In addition, it was observed that fivefold Ti cations behaved as $3d^0$ bulk cations, showing no spin population, proving that the dangling bonds were the main effects of the unusual Ti magnetism.

The cutting process linked to the surface structures generated different kinds of undercoordinated centers from the existence of dangling bonds—an inherent process associated with the symmetry-adapted cutting strategy without any changes to the crystal stoichiometry. In this case, the exposed local geometries were notably different compared to the bulk. In this study, the investigated surfaces could exhibit three kinds of undercoordinated clusters: $[MO_5]$, $[MO_4]$, and $[MO_3]$ (M = Mn, Ti). Considering the electron density reorganization on the cut surfaces, the metal undercoordinated degree modified the energy-level distribution in the VB, as presented in Fig. 3. Therefore, the intervalence charge-transfer that is responsible for the enhanced surface magnetism and magnetic Ti species could be understood from the electronic disorder associated with oxygen valence orbitals linked to the $[MnO_nV_o^x] - [TiO_nV_o^x]$ bond path. Fig. 4 schematically represents the existence of one, two, and three dangling bonds in the investigated surfaces, which induces the perturbation on the energy levels of the remaining atoms.

The combination of DOS (Fig. 3) and spin-population analysis (Table 2 and Fig. 3) enables us to note that the existence of dangling bonds in the investigated surfaces created intermediary levels in the

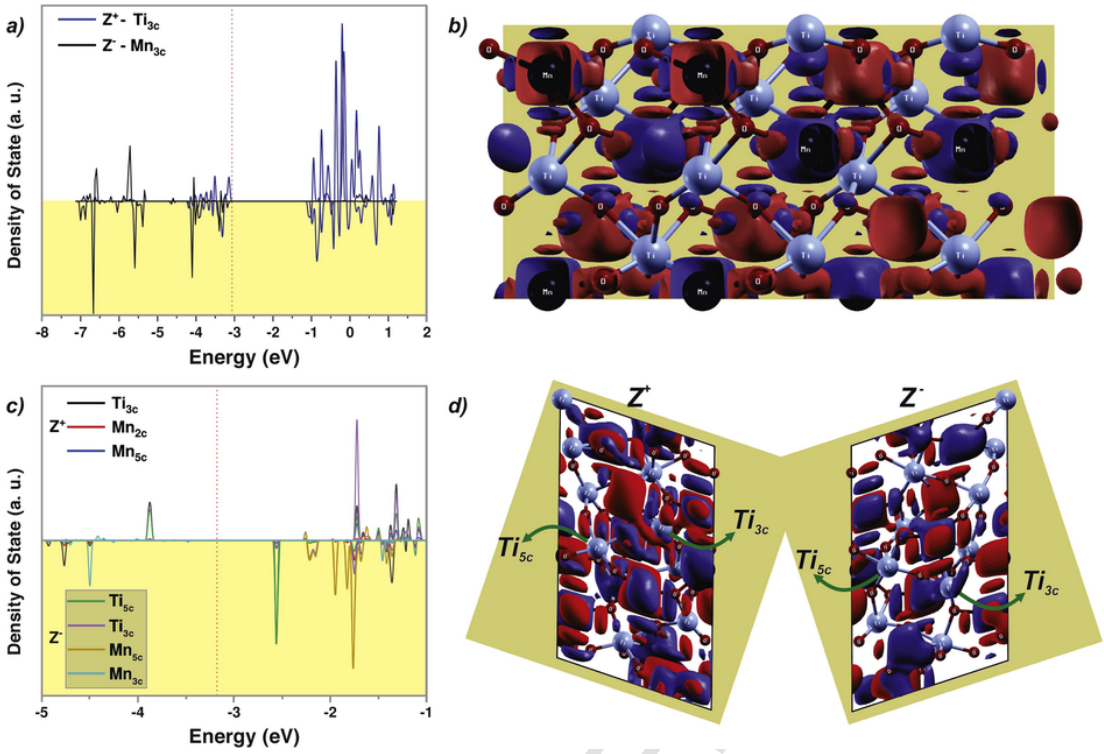

Fig. 3. Projections of the density of states (a, c) and spin densities (b,d) for (0 0 1) and (1 1 1) surfaces. The black, blue, and red balls represent Mn, Ti, and O ions, respectively. Blue and red surfaces correspond to spin-up and spin-down densities. (For interpretation of the references to colour in this figure legend, the reader is referred to the web version of this article.)

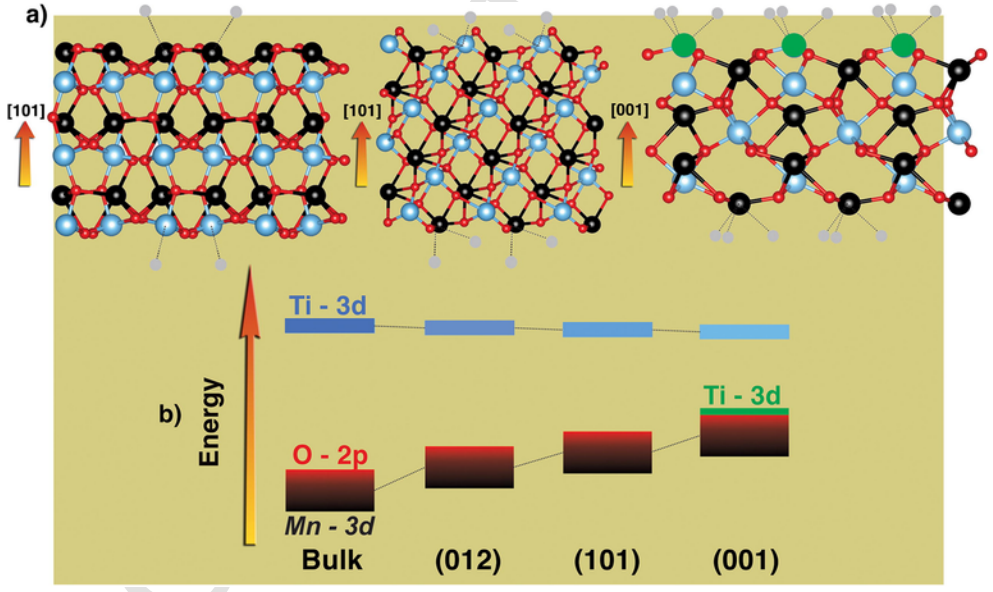

Fig. 4. Scheme to represent the local geometries for (a) (0 1 2), (1 0 1) and (0 0 1) surfaces and its (b) Energy-level diagram. The black, blue, red and green balls represent Mn^{2+}, Ti^{4+}, O^{2-} and Ti^{3+} ions, respectively. The dashed bonds represent the dangling bonds. (For interpretation of the references to colour in this figure legend, the reader is referred to the web version of this article.)

vicinity of the bandgap region compared to the bulk. Thus, local disorder associated with undercoordinated cations increased the VB energy through changes in Mn (3d) crystal-field energy splitting summed to the electronic reordering with increased energy of remaining O (2p) orbitals. With increasing number of dangling bonds, the upper part of VB drastically changed, mainly because the energy of occupied 2p states increased, enabling the enhancement of the $[MnO_nV_o^x] - [TiO_nV_o^x]$ bond path, which stabilized the occupation of Ti (3d) orbitals.

In addition, by analyzing the local environment of reduced Ti clusters, it was observed that oxygen atoms from subsurface layers moved toward the exposed Ti atom to redistribute the electron density along the surface. On the other hand, the local arrangement for subsuperficial [MnO_6] clusters changed owing to the existence of a stronger $[MnO_nV_o^x] - [TiO_nV_o^x]$ bond path. It was then possible to assume an oxygen-mediated charge transfer between the [MnO_n] and [TiO_n] ($n = 4$, 5, 6) clusters using the Kroger–Vink notation [59]. In this formalism, the charge accumulation mechanism could be described using the neu-

tral $[MO_n]^x$, positively charged $[MO_nV_O^{\bullet}]^{\bullet}$, and negatively charged $[MO_n]'$ cluster notation. In this case, the charge-transfer mechanism was as follows:

$$[MnO_n]^x + [TiO_n]^x \rightarrow [TiO_n]' + [MnO_{n-1} \ldots V_O]^{\cdot}$$

Therefore, the perturbation on the VBM was attributed to the increase of oxygen (2p) energy levels, which behaved as positively-charged vacancies in subsuperficial $[MnO_n]$ clusters that became $[MnO_{n-1}\ldots V_O^{\bullet}]^{\bullet}$, resulting in stronger $[MnO_nV_o^x] - [TiO_nV_o^x]$bond path that enabled a charge accumulation on superficial $[TiO_n]'$ clusters for (0 0 1) and (1 1 1) surfaces.

Furthermore, the obtained results suggest that the creation of oxygen vacancies in these surfaces could also contribute to enhance the magnetic moment along the planes, owing to the combination of the dangling bond effect and electron trapping from missing atoms, as reported for other materials [58,60]. This topic will be investigated in forthcoming studies.

3.3. Superficial magnetism and crystal morphology

In this section, we investigate the $MnTiO_3$ crystal morphology by employing the Wulff construction [61], in which the values of E_{surf} for each surface determine the final morphology. The Wulff proposal refers to a simple relation between E_{surf} and the distance in the normal direction from the center of the crystallite, which also allows this ideal morphology to be modified by tuning the surface energies of the different facets [62,63]. In recent years, this method was successfully applied for different kinds of materials, showing excellent agreement between theoretical predicted and experimental reported morphologies [45,64–67].

Recently, we proposed a theoretical procedure to rationalize the relation between superficial magnetism and crystal morphologies by combining the Wulff construction model with spin analysis along the surface planes, providing a different perspective to understand the uncompensated spins responsible for unusual magnetic properties of Co_3O_4 [68]. Here, this method was employed to investigate the magnetic properties of shape-controlled $MnTiO_3$ material.

First, the complete set of available morphologies for the multiferroic $MnTiO_3$ material are summarized in Fig. 5, in which the transformations were obtained by tuning the surface energies of the different facets. It is important to note that the E_{surf} values used to obtain the different morphologies correspond to a mean value between the complementary terminations, E_{cleav}^{relax}, presented in Table 1.

The *vacuum* ideal morphology proposed by $MnTiO_3$ exhibited a corner-truncated cylindrical shape that predominantly exposed the (1 1 0) surface and, to a minor extent, the (0 1 2) and (0 0 1) surfaces. Despite the higher value of E_{surf} for (0 0 1) surface, the ideal morphology of $MnTiO_3$ showed an extent of this plane, suggesting the existence of intriguing magnetic behavior due to the exposure of unusual magnetic Ti species, as previously discussed. In addition, it was observed that dif-

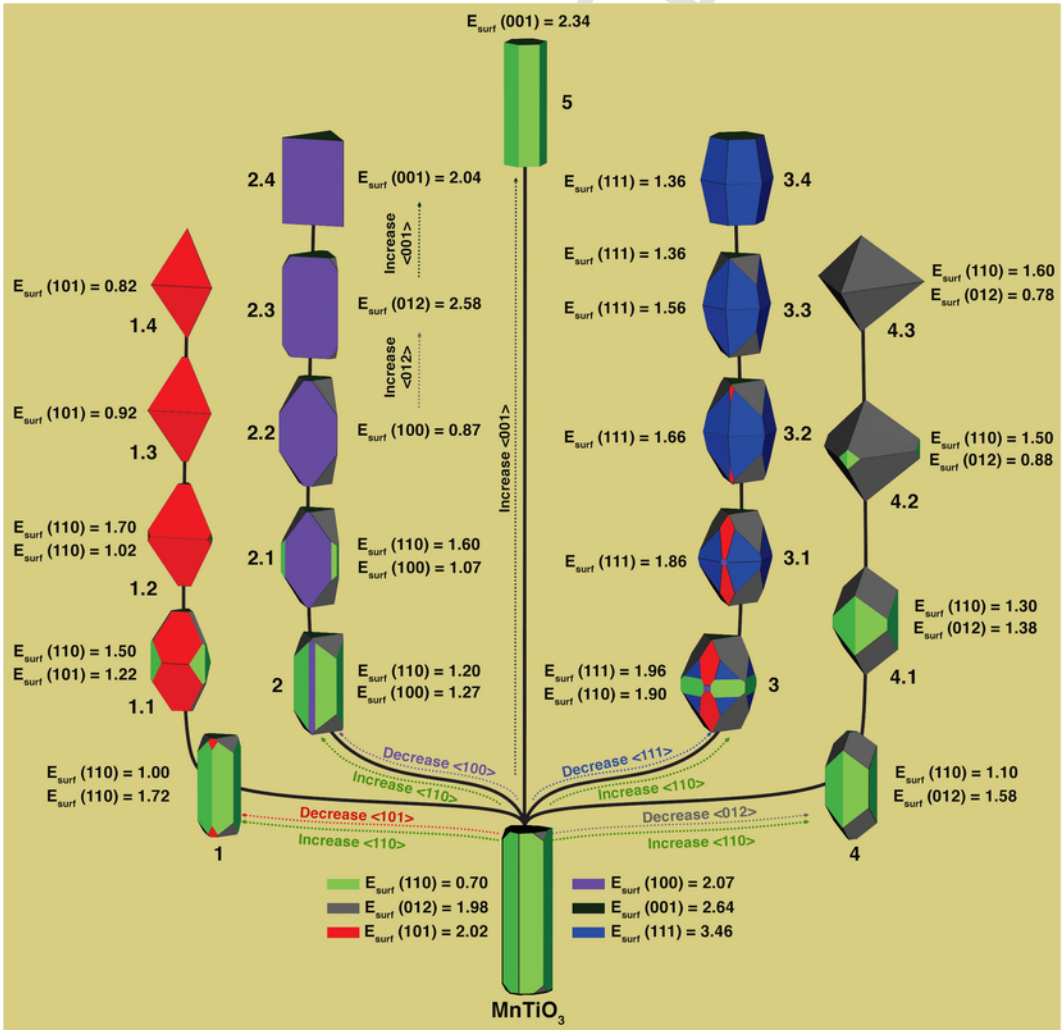

Fig. 5. Complete set of available morphologies of $MnTiO_3$ considering the (1 1 0), (0 1 2), (1 0 1), (1 0 0), (0 0 1) and (1 1 1) surfaces. Values of surface energy, (E_{surf}), in J/m^2.

ferent shapes were obtained by tuning E_{surf} for $MnTiO_3$, such as truncated and nontruncated cylindrical, octahedral, rhombic, and monoclinic shapes. However, no research has reported the synthetic control of crystal morphology for $MnTiO_3$, making difficult the deeper comparison between theoretical and experimental morphologies.

To rationalize the superficial magnetism in such morphologies, we performed a summation between the magnetic moments along the surface planes, respecting the experimental G-type antiferromagnetic ordering. The magnetization density (D_μ) index of a given surface was calculated (*Supporting Information*), considering the magnetic moment (μ_B) per unit cell area (A):

$$D_\mu = \frac{\mu_B}{A} \quad (4)$$

Further, the magnetization density (M) index of a given morphology was obtained by combining the polyhedron composition (c_{hkl}) and the magnetization density (D_μ):

$$M = \sum c_{(hkl)} \bullet D_\mu^{(hkl)} \quad (5)$$

Table 3
Surface contribution and total magnetization density (M) index calculated for the different $MnTiO_3$ morphologies.

Morphologies	Surface contribution (%)						M (μ_B nm^{-2})
	(110)	(012)	(101)	(100)	(001)	(111)	
Ideal	71.8	1.8	–	–	26.4	–	5.53
1	63.1	10.5	2.8	–	23.6	–	5.00
1.1	13.2	5.7	70.6	–	10.5	–	2.24
1.2	0.9	–	95.7	–	3.4	–	0.72
1.3	–	–	99.0	–	1.0	–	0.21
1.4	–	–	100.0	–	–	–	0.00
2	43.3	16.9	–	19.8	20.1	–	4.31
2.1	3.5	15.0	–	68.1	13.3	–	2.89
2.2	–	8.8	–	79.0	12.2	–	2.62
2.3	–	0.8	–	80.0	19.1	–	3.99
2.4	–	–	–	75.7	24.3	–	5.06
3	15.5	40.0	17.8	1.4	18.1	7.2	4.11
3.1	–	40.1	14.4	1.2	21.3	22.9	4.87
3.2	–	31.9	2.0	–	26.3	39.8	5.96
3.3	–	25.5	–	–	28.9	45.6	6.51
3.4	–	–	–	–	18.7	81.3	4.43
4	58.3	39.7	–	–	1.9	–	0.68
4.1	40.4	59.6	–	–	–	–	0.42
4.2	3.3	96.7	–	–	–	–	0.68
4.3	0.0	100.0	–	–	–	–	0.70
5	68.9	–	–	–	31.1	–	6.48

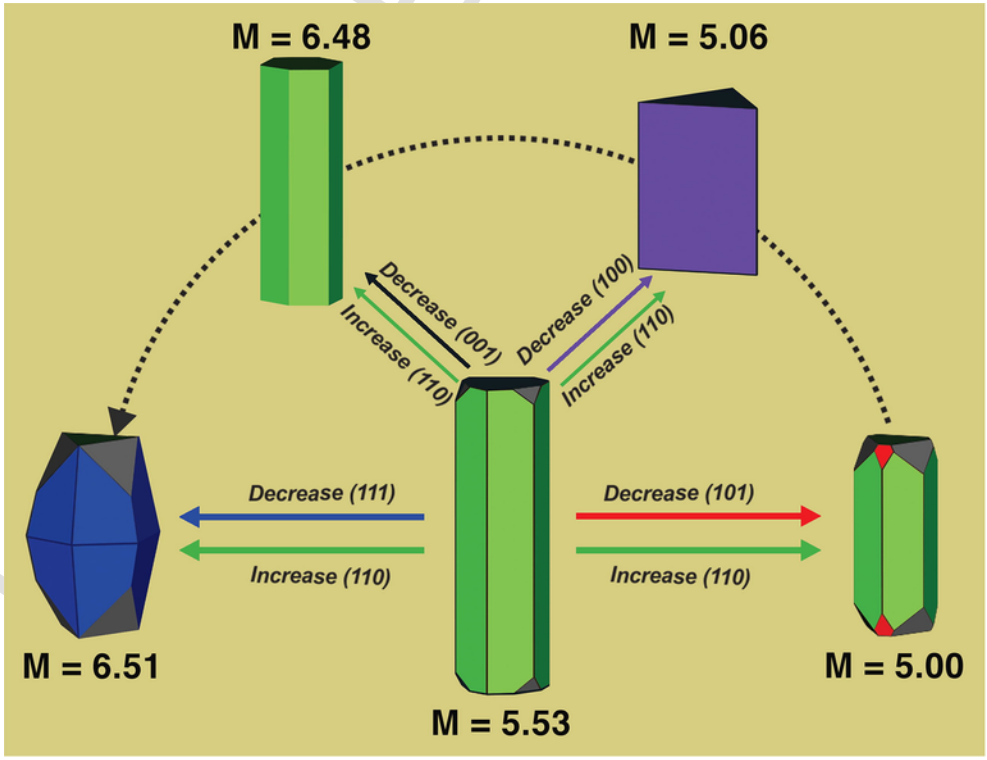

Fig. 6. Morphology modulation of multiferroic $MnTiO_3$ material considering the total magnetization density (M). The dashed black line indicates the increasing of M related to the control of (001) surface area composition.

The total magnetization density (*M*) for the different shapes reported in Fig. 4 are summarized in Table 3, where the contribution of each surface (%) on M is listed.

Regarding the superficial magnetism for the different morphologies predicted for $MnTiO_3$ (Fig. 5), it was observed that all *M* values were obtained by combining the uncompensated spins of (0 1 2), (0 0 1), and (1 1 1) surfaces, in agreement with the spin populations presented in Table 2. In addition, the increased superficial magnetism of some polyhedrons (higher *M* values) was attributed to the contribution of the (0 0 1) surface due to the higher magnetic moment along the surface plane. From a technological point of view, this result is exciting because the control of (0 0 1) surface properties of many perovskite (ABO_3) materials has been intensively explored during recent years. Moreover, some reports for multiferroic $BiFeO_3$ based-material show the existence of a (0 0 1) surface plane in the reported morphologies, and the z-cut of $LiNbO_3$ (R3c) exhibits an intriguing mechanism associated with the dependence of ferroelectric ordering [10,69–71].

The precise control of superficial magnetism for antiferromagnetic multiferroic materials is important to increase the magnetoelectric coupling in such compounds. Here, we argue that the (0 0 1) surface orientation, which exhibits a large ferroelectric tensor, shows an enhanced magnetic moment. Thereby, this result allows us to predict that polar distortions along the (0 0 1) direction can control the superficial magnetism through the exposure of undercoordinated cations, once the ferroelectric distortion involves the cationic displacement of A and Ti cations along this direction. By combining the values for the surface energy (E_{surf}) and total magnetization density (*M*), it is possible to obtain a morphology map that summarizes the highest values of *M* following the percentage of (0 0 1) surface area composition, as depicted in Fig. 6.

In this way, the shape-oriented multiferroic nanoparticles could present a superior magnetoelectric effect from the reorientation of the crystalline structure, which induces a different spin distribution along the material surfaces.

4. Conclusions

In this work, first-principles DFT calculations have been performed to investigate the stoichiometric polar and nonpolar surfaces for the R3c multiferroic $MnTiO_3$. The surface stability, in order of increasing surface energy, for the low index surfaces of $MnTiO_3$ was found to be (1 1 0) > (0 1 2) > (1 0 1) > (1 0 0) > (0 0 1) > (1 1 1), with the most stable surfaces having both high Ti and Mn surface coordination. Electronic and magnetic properties of the different surfaces were investigated by a simple procedure, without surface reconstructions or chemical adsorptions showing evidence for the presence of an enhanced magnetic moment at cleaved surfaces that is capable to clarify their multiferroic nature. A deep analysis of the superficial uncompensated spin, especially for unstable (0 0 1) and (1 1 1) surfaces, shows the presence of magnetic Ti species. This intriguing result was explained rationally by the crystal-field energy scales in the cleaved surface environments associated with the presence of different local Ti and Mn coordinations. To the best of our knowledge, we report the first study about the morphological modulations of multiferroic material. The calculated equilibrium morphology is elongated along the c-axis, showing a hexagonal corner-truncated cylindrical shape containing nonpolar (1 1 0) and polar (0 1 2) and (0 0 1) surfaces. Furthermore, by controlling the ratio between the calculated surface energies, a morphological map for $MnTiO_3$ was predicted. By combining the morphological map with the singular spin densities associated with the surfaces, it was found that the exposure of the (0 0 1) surface plane is mandatory to increase the superficial magnetism and the magnetoelectric coupling for $MnTiO_3$ nanoparticles, enabling us to conclude that superior multiferroic properties and exciting applications can be obtained from the morphological control of $MnTiO_3$.

5. Author contributions

The manuscript was written through contributions of all authors. All authors have given approval to the final version of the manuscript. These authors contributed equally.

Acknowledgment

This work was supported by the State University of Ponta Grossa, University of Jaume I, CAPES, PDSE-CAPES and Fundação Araucária. J. A. acknowledges the financial support of the following agencies: Generalitat Valenciana for PrometeoII/2014/022, Prometeo/2016/079, ACOMP/2014/270, ACOMP/2015/1202, Ministerio de Economia y Competitividad, project CTQ2015-65207-P. E. Longo acknowledges the financial support of FAPESP 2013/07296-2. R. Ribeiro thanks to assistant professor Lourdes Gracia from Department of Physical Chemistry – University of Valencia by expertise and discussions about surfaces.

Appendix A. Supplementary material

Supplementary data associated with this article can be found, in the online version, at https://doi.org/10.1016/j.apsusc.2018.05.067.

References

[1] J. Goniakowski, F. Finocchi, C. Noguera, Polarity of oxide surfaces and nanostructures, Rep. Prog. Phys. 71 (2008) 016501.
[2] K. Garrity, A.M. Kolpak, S. Ismail-Beigi, E.I. Altman, Chemistry of ferroelectric surfaces, Adv. Mater. 22 (2010) 2969–2973.
[3] A. Kakekhani, S. Ismail-Beigi, E.I. Altman, Ferroelectrics: a pathway to switchable surface chemistry and catalysis, Surf. Sci. 650 (2016) 302–316.
[4] A. Kakekhani, S. Ismail-Beigi, Ferroelectric-based catalysis: switchable surface chemistry, ACS Catal. 5 (2015) 4537–4545.
[5] S.V. Kalinin, D.A. Bonnell, T. Alvarez, X. Lei, Z. Hu, J.H. Ferris, Q. Zhang, S. Dunn, Atomic polarization and local reactivity on ferroelectric surfaces: a new route toward complex nanostructures, Nano Lett. 2 (2002) 589–593.
[6] M.A. Khan, M.A. Nadeem, H. Idriss, Ferroelectric polarization effect on surface chemistry and photo-catalytic activity: a review, Surf. Sci. Rep. 71 (2016) 1–31.
[7] S. Kim, M.R. Schoenberg, A.M. Rappe, Polarization dependence of palladium deposition on ferroelectric lithium niobate (0 0 0 1) surfaces, Phys. Rev. Lett. 107 (2011) 076102.
[8] M.N. Liu, D.F. Xue, C. Yan, J. Bell, Facile synthesis of lithium niobate from novel precursor $H_2(H_2O)NB_2O_6$, Mater. Technol. 27 (2014) 92–94.
[9] F. Merola, S. Grilli, S. Coppola, V. Vespini, S. De Nicola, P. Maddalena, C. Carfagna, P. Ferraro, Reversible fragmentation and self-assembling of nematic liquid crystal droplets on functionalized pyroelectric substrates, Adv. Funct. Mater. 22 (2012) 3267–3272.
[10] S. Sanna, W.G. Schmidt, $LiNbO_3$ surfaces from a microscopic perspective, J. Phys. Condens. Matter : Institute Phys. J. 29 (2017) 413001.
[11] M. Stock, S. Dunn, Influence of the ferroelectric nature of lithium niobate to drive photocatalytic dye decolorization under artificial solar light, J. Phys. Chem. C 116 (2012) 20854–20859.
[12] S. Deng, S. Cheng, C. Xu, B. Ge, X. Sun, R. Yu, W. Duan, J. Zhu, Atomic mechanism of hybridization-dependent surface reconstruction with tailored functionality in hexagonal multiferroics, ACS Appl. Mater. Interfaces 9 (2017) 27322–27331.
[13] G. Catalan, J.F. Scott, Physics and applications of bismuth ferrite, Adv. Mater. 21 (2009) 2463–2485.
[14] L. Zhu, K.L. Yao, Z.L. Liu, D.H. Zhang, Stability and electronic structure of $BiFeO_3$ (1 1 1) polar surfaces by first-principle calculations, Phys. Lett. A 373 (2009) 2374–2381.
[15] T. Shimada, K. Arisue, J. Wang, T. Kitamura, Ab initiostudy of multiferroic $BiFeO_3$(1 1 0) surfaces, Phys. Rev. B 89 (2014).
[16] J.-Q. Dai, J.-W. Xu, J.-H. Zhu, First-principles study on the multiferroic $BiFeO_3$ (0 0 0 1) polar surfaces, Appl. Surf. Sci. 392 (2017) 135–143.
[17] J.-Q. Dai, J.-W. Xu, J.-H. Zhu, Thermodynamic Stability of $BiFeO_3$ (0 0 0 1) Surfaces from ab Initio Theory, ACS Appl. Mater. Interfaces 9 (2017) 3168–3177.
[18] J.-Q. Dai, J.-H. Zhu, J.-W. Xu, First-principles investigation of platinum monolayer adsorption on the $BiFeO_3$ (0 0 0 1) polar surfaces, Appl. Surf. Sci. 428 (2018) 964–971.
[19] C. Ederer, C.J. Fennie, Electric-field switchable magnetization via the Dzyaloshinskii-Moriya interaction: $FeTiO_3$ versus $BiFeO_3$, J. Phys.: Condens. Matter 20 (2008) 434219.
[20] C.J. Fennie, Ferroelectrically induced weak ferromagnetism by design, Phys. Rev. Lett. 100 (2008) 167203.

[21] T. Varga, A. Kumar, E. Vlahos, S. Denev, M. Park, S. Hong, T. Sanehira, Y. Wang, C.J. Fennie, S.K. Streiffer, X. Ke, P. Schiffer, V. Gopalan, J.F. Mitchell, Coexistence of weak ferromagnetism and ferroelectricity in the high pressure $LiNbO_3$-type phase of $FeTiO_3$, Phys. Rev. Lett. 103 (2009) 047601.

[22] T. Varga, T.C. Droubay, M.E. Bowden, R.J. Colby, S. Manandhar, V. Shutthanandan, D. Hu, B.C. Kabius, E. Apra, W.A. Shelton, S.A. Chambers, Coexistence of weak ferromagnetism and polar lattice distortion in epitaxial $NiTiO_3$ thin films of the $LiNbO_3$-type structure, J. Vacuum Sci. Technol. B Nanotechnol. Microelectron.: Mater. Process. Measure. Phenomena 31 (2013) 030603.

[23] T. Varga, T.C. Droubay, L. Kovarik, M.I. Nandasiri, V. Shutthanandan, D. Hu, B. Kim, S. Jeon, S. Hong, Y. Li, S.A. Chambers, Coupled lattice polarization and ferromagnetism in multiferroic $NiTiO_3$ thin films, ACS Appl. Mater. Interfaces 9 (2017) 21879–21890.

[24] A.M. Arévalo-López, J.P. Attfield, Weak ferromagnetism and domain effects in multiferroic $LiNbO_3$-type $MnTiO_3$-II, Phys. Rev. B 88 (2013).

[25] R.A.P. Ribeiro, S.R. de Lazaro, C. Gatti, The role of exchange–correlation functional on the description of multiferroic properties using density functional theory: the $ATiO_3$ (A = Mn, Fe, Ni) case study, RSC Adv. 6 (2016) 101216–101225.

[26] N. Mufti, G.R. Blake, M. Mostovoy, S. Riyadi, A.A. Nugroho, T.T.M. Palstra, Magnetoelectric coupling in $MnTiO_3$, Phys. Rev. B 83 (2011).

[27] X. Hao, Y. Xu, C. Franchini, F. Gao, Covalent effects in magnetic ferroelectrics MnMO3 (M = Ti, Sn), Phys. Status Solidi (b), 252 (2015) 626–634.

[28] P.W. Tasker, The stability of ionic crystal surfaces, J. Phys. C: Solid State Phys. 12 (1979) 4977.

[29] R.I. Eglitis, D. Vanderbilt, Ab initiocalculations of $BaTiO_3$ and $PbTiO_3$(0 0 1) and (0 1 1) surface structures, Phys. Rev. B 76 (2007).

[30] R.I. Eglitis, M. Rohlfing, First-principles calculations of the atomic and electronic structure of $SrZrO_3$ and $PbZrO_3$ (0 0 1) and (0 1 1) surfaces, J. Phys. Condens. Matter : Institute Phys. J. 22 (2010) 415901.

[31] R.I. Eglitis, Comparativeab initiocalculations of SrTiO3 and CaTiO3 polar (1 1 1) surfaces, Phys. status solidi (b), 252 (2015) 635–642.

[32] D. Blanck, E. Berrier, J.-F. Paul, First-principles investigation of the relevant surfaces exposed by polycrystalline $LaFeO_3$, ChemCatChem 9 (2017) 2383–2389.

[33] D. Mora-Fonz, T. Lazauskas, M.R. Farrow, C.R.A. Catlow, S.M. Woodley, A.A. Sokol, Why are polar surfaces of ZnO stable?, Chem. Mater. 29 (2017) 5306–5320.

[34] X. Tian, T. Wang, L. Fan, Y. Wang, H. Lu, Y. Mu, A DFT based method for calculating the surface energies of asymmetric MoP facets, Appl. Surf. Sci. 427 (2018) 357–362.

[35] F. Viñes, G. Konstantatos, F. Illas, Matildite contact with media: first-principles study of $AgBiS_2$ surfaces and nanoparticle morphology, J. Phys. Chem. B 122 (2018) 521–526.

[36] R. Dovesi, R. Orlando, A. Erba, C.M. Zicovich-Wilson, B. Civalleri, S. Casassa, L. Maschio, M. Ferrabone, M. De La Pierre, P. D'Arco, Y. Noël, M. Causà, M. Rérat, B. Kirtman, CRYSTAL14: a program for theab initioinvestigation of crystalline solids, Int. J. Quantum Chem. 114 (2014) 1287–1317.

[37] C. Adamo, V. Barone, Toward reliable density functional methods without adjustable parameters: the PBE0 model, J. Chem. Phys. 110 (1999) 6158–6170.

[38] I. de P.R. Moreira, R. Dovesi, C. Roetti, V.R. Saunders, R. Orlando, Ab initio study of MF2 (M = Mn,Fe,Co,Ni) rutile-type compounds using the periodic unrestricted Hartree-Fock approach, Phys. Rev. B, 62 (2000) 7816–7823.

[39] F. Corà*, The performance of hybrid density functionals in solid state chemistry: the case of $BaTiO_3$, Mol. Phys. 103 (2005) 2483–2496.

[40] M.D. Towler, N.L. Allan, N.M. Harrison, V.R. Saunders, W.C. Mackrodt, E. Aprà, Ab initio study of MnO and NiO, Phys. Rev. B 50 (1994) 5041–5054.

[41] H.J. Monkhorst, J.D. Pack, Special points for Brillouin-zone integrations, Phys. Rev. B 13 (1976) 5188–5192.

[42] M.M. Ferrer, A.F. Gouveia, L. Gracia, E. Longo, J. Andrés, A 3D platform for the morphology modulation of materials: first principles calculations on the thermodynamic stability and surface structure of metal oxides: Co_3O_4, α-Fe_2O_3, and In_2O_3, Model. Simul. Mater. Sci. Eng. 24 (2016) 025007.

[43] L. Wang, F. Zhou, Y.S. Meng, G. Ceder, First-principles study of surface properties of $LiFePO_4$: surface energy, structure, Wulff shape, and surface redox potential, Phys. Rev. B 76 (2007) 165435.

[44] Z.-Y. Gao, W. Sun, Y.-H. Hu, Mineral cleavage nature and surface energy: anisotropic surface broken bonds consideration, Trans. Nonferrous Metals Soc. China 24 (2014) 2930–2937.

[45] A.F. Gouveia, M.M. Ferrer, J.R. Sambrano, J. Andrés, E. Longo, Modeling the atomic-scale structure, stability, and morphological transformations in the tetragonal phase of $LaVO_4$, Chem. Phys. Lett. 660 (2016) 87–92.

[46] E.A. Ahmad, G. Mallia, D. Kramer, A.R. Kucernak, N.M. Harrison, The stability of $LaMnO_3$ surfaces: a hybrid exchange density functional theory study of an alkaline fuel cell catalyst, J. Mater. Chem. A 1 (2013) 11152–11162.

[47] S. Zhou, E. Čižmár, K. Potzger, M. Krause, G. Talut, M. Helm, J. Fassbender, S.A. Zvyagin, J. Wosnitza, H. Schmidt, Origin of magnetic moments in defective TiO_2 single crystals, Phys. Rev. B 79 (2009) 113201.

[48] G.B. Soares, R.A.P. Ribeiro, S.R. de Lazaro, C. Ribeiro, Photoelectrochemical and theoretical investigation of the photocatalytic activity of TiO_2:N, RSC Adv. 6 (2016) 89687–89698.

[49] M. Xing, W. Fang, M. Nasir, Y. Ma, J. Zhang, M. Anpo, Self-doped Ti^{3+}-enhanced TiO_2 nanoparticles with a high-performance photocatalysis, J. Catal. 297 (2013) 236–243.

[50] N.A. Deskins, R. Rousseau, M. Dupuis, Distribution of Ti^{3+} Surface Sites in Reduced TiO_2, J. Phys. Chem. C 115 (2011) 7562–7572.

[51] C. Di Valentin, G. Pacchioni, A. Selloni, Reduced and n-type doped TiO_2: nature of Ti^{3+} species, J. Phys. Chem. C 113 (2009) 20543–20552.

[52] M.O.J.Y. Hunault, W. Khan, J. Minár, T. Kroll, D. Sokaras, P. Zimmermann, M.U. Delgado-Jaime, F.M.F. De Groot, Local vs nonlocal states in $FeTiO_3$ probed with 1s2pRIXS: implications for photochemistry, Inorg. Chem. 56 (2017) 10882–10892.

[53] T. Fujii, M. Yamashita, S. Fujimori, Y. Saitoh, T. Nakamura, K. Kobayashi, J. Takada, Large magnetic polarization of Ti^{4+} ions in $FeTiO_3$, J. Magn. Magn. Mater. 310 (2007) e555–e557.

[54] A. Agui, M. Mizumaki, T. Uozumi, Intermetallic charge transfer in $MTiO_3$ (M = Mn, Fe Co, and Ni) by Ti 2p edge resonant inelastic X-ray scattering, J. Electron. Spectrosc. Relat. Phenom. 205 (2015) 106–110.

[55] T. Seda, G.R. Hearne, Pressure induced $Fe^{2+} + Ti^{4+} \rightarrow Fe^{3+} + Ti^{3+}$ intervalence charge transfer and the Fe^{3+}/Fe^{2+} ratio in natural ilmenite ($FeTiO_3$) minerals, J. Phys.: Condens. Matter 16 (2004) 2707–2718.

[56] R.A.P. Ribeiro, S.R. de Lazaro, Structural, electronic and elastic properties of $FeBO_3$ (B = Ti, Sn, Si, Zr) ilmenite: a density functional theory study, RSC Adv. 4 (2014) 59839–59846.

[57] D. Qian, Y. Hinuma, H. Chen, L.-S. Du, K.J. Carroll, G. Ceder, C.P. Grey, Y.S. Meng, Electronic Spin Transition in Nanosize Stoichiometric Lithium Cobalt Oxide, J. Am. Chem. Soc. 134 (2012) 6096–6099.

[58] D.A. Tompsett, S.C. Parker, M.S. Islam, Surface properties of alpha-MnO_2: relevance to catalytic and supercapacitor behavior, J. Mater. Chem. A 2 (2014) 15509–15518.

[59] F.A. Kröger, H.J. Vink, Relations between the concentrations of imperfections in crystalline solids, in: F. Seitz, D. Turnbull (Eds.), Solid State Physics, Academic Press, 1956, pp. 307–435.

[60] A.L. Gavin, G.W. Watson, Modeling oxygen defects in orthorhombic $LaMnO_3$ and its low index surfaces, PCCP 19 (2017) 24636–24646.

[61] The Wulff theorem, in: R. Cerf, J. Picard (Eds.) The Wulff Crystal in Ising and Percolation Models: Ecole d'Eté de Probabilités de Saint-Flour XXXIV - 2004, Springer Berlin Heidelberg, Berlin, Heidelberg, 2006, pp. 189–199.

[62] G.D. Barmparis, Z. Lodziana, N. Lopez, I.N. Remediakis, Nanoparticle shapes by using Wulff constructions and first-principles calculations, Beilstein J. Nanotechnol. 6 (2015) 361–368.

[63] J. Andrés, L. Gracia, A.F. Gouveia, M.M. Ferrer, E. Longo, Effects of surface stability on the morphological transformation of metals and metal oxides as investigated by first-principles calculations, Nanotechnology 26 (2015) 405703.

[64] G. Byzynski, C. Melo, D.P. Volanti, M.M. Ferrer, A.F. Gouveia, C. Ribeiro, J. Andrés, E. Longo, The interplay between morphology and photocatalytic activity in ZnO and N-doped ZnO crystals, Mater. Des. 120 (2017) 363–375.

[65] V.M. Longo, L. Gracia, D.G. Stroppa, L.S. Cavalcante, M. Orlandi, A.J. Ramirez, E.R. Leite, J. Andrés, A. Beltrán, J.A. Varela, E. Longo, A joint experimental and theoretical study on the nanomorphology of $CaWO_4$ crystals, J. Phys. Chem. C 115 (2011) 20113–20119.

[66] M.C. Oliveira, L. Gracia, M. de Assis, I.L.V. Rosa, M.F. do Carmo Gurgel, E. Longo, J. Andrés, Mechanism of photoluminescence in intrinsically disordered $CaZrO_3$ crystals: first principles modeling of the excited electronic states, J. Alloy. Compd. 722 (2017) 981–995.

[67] P.F.S. Pereira, C.C. Santos, A.F. Gouveia, M.M. Ferrer, I.M. Pinatti, G. Botelho, J.R. Sambrano, I.L.V. Rosa, J. Andrés, E. Longo, α-$Ag_{2-2x}Zn_xWO_4$ ($0 \leq x \leq 0.25$) solid solutions: structure, morphology, and optical properties, Inorg. Chem. 56 (2017) 7360–7372.

[68] R.A.P. Ribeiro, S.R.d. Lazaro, L. Gracia, E. Longo, J. Andrés, Theoretical approach for determining the relation between the morphology and surface magnetism of Co3O4, *J. Mag. Magnet. Mater.* **453**, 2018, 262-267.

[69] L. Hou, Z.Y. Lu, Y.C. Dai, K.H. Zuo, Y.F. Xia, Z.M. Ren, J. Wu, X.G. Lu, Y.P. Zeng, X. Li, Self-assembled growth of $BiFeO_3$ meso-octahedral particles synthesized by a facile surfactant-free hydrothermal method, J. Cryst. Growth 434 (2016) 42–46.

[70] Y. Lv, J. Xing, C. Zhao, D. Chen, J. Dong, H. Hao, X. Wu, Z. Zheng, The effect of solvents and surfactants on morphology and visible-light photocatalytic activity of $BiFeO_3$ microcrystals, J. Mater. Sci.: Mater. Electron. 26 (2015) 1525–1532.

[71] X. Xu, Q. Xu, Y. Huang, X. Hu, Y. Huang, G. Wang, X. Hu, N. Zhuang, Control of crystal phase and morphology in hydrothermal synthesis of $BiFeO_3$ crystal, J. Cryst. Growth 437 (2016) 42–48.